Projected Amazon forest loss alters tropical Atlantic circulation and surface heat exchange through reduced freshwater input

Nelson Almeida Gouveia
nelsongov89@gmail.com

University of Victoria

Sly Wongchuig
Université de Toulouse, LEGOS (CNES/CNRS, IRD/UT3)

Jhan-Carlo Espinoza
University of Grenoble Alpes, IRD, CNRS, Grenoble INP, UMR 5001)

Luiz E. O. C. Aragão
National Institute for Space Research (INPE)

Eduardo Tavares Paes
Federal Rural University of Amazon

Ramon Batista Santos
National Institute for Space Research (INPE)

Douglas F. M. Gherardi
National Institute for Space Research (INPE)

Article

Keywords: Amazon deforestation, river discharge, river-ocean interaction

Posted Date: June 4th, 2026

DOI: https://doi.org/10.21203/rs.3.rs-9752662/v1

Additional Declarations: No competing interests reported.

Abstract

Deforestation alters the terrestrial water cycle, with growing implications for land–ocean connections. In the Amazon Basin, projected forest loss is expected to substantially modify river discharge, yet how these hydrological changes affect tropical ocean circulation and surface heat exchange remains poorly understood. Here we conducted offline a hydrological simulation using the Great Basin Model (GBM) to produce river outflow for a business-as-usual deforestation scenario projected for 2050, that was fed into the Regional Ocean Model System (ROMS) simulating the ocean for the period 1992–2015. This modeling setup allowed us to assess how changes in freshwater export influence the western tropical North Atlantic. Simulations of a business-as-usual 2050 scenario (~ 45% forest loss) show dry-season discharge reductions exceeding 50% in southern tributaries and ~ 12% at Óbidos, increasing surface salinity and reorganizing the Amazon River plume. These changes intensify the North Brazil Current and its retroflection by ~ 14%, deepen the mixed layer by up to ~ 8 m, thin the barrier layer by 5–10 m, and alter surface heat exchange, producing seasonally contrasting sea-surface temperature anomalies. Our results indicate that sustained Amazon forest loss can drive persistent changes in the upper-ocean circulation and heat distribution of the tropical Atlantic.

Introduction

The Amazon River Basin (ARB) has undergone an alarming rate of deforestation over the past three decades, resulting in the loss of more than 20% of its original forest cover (1, 2). The main drivers include agricultural expansion, particularly cattle ranching and soybean cultivation (3, 4), illegal logging and fires (5), and unregulated mining (6). While cattle ranching remains the dominant driver, soybean expansion into native forests accounted for roughly 30% of all forest loss in the mid-2000s (7, 8). Beyond the direct reduction in forest area, these processes disturb the hydrological cycle not only within the basin but also across the broader atmosphere–land–ocean continuum (9, 10). Observations under current deforestation levels (~ 20% forest loss) show intensified runoff and increased river discharge, which freshen and warm the western tropical North Atlantic (11). Modeling studies suggest that when deforestation surpasses 40%, the feedback between vegetation, precipitation, and runoff amplifies, producing nonlinear alterations in the hydrological cycle and in the frequency of extreme events (12). Non-local factors such as warm anomalies in the North Tropical Atlantic and La Niña events in the Pacific have also been linked to major floods in the Amazon (13). Despite this growing understanding of land–climate interactions, the consequences of future deforestation for the oceanic domain remain poorly quantified.

At the catchment scale (< 100 km²), deforestation enhances surface runoff and subsurface drainage while reducing evapotranspiration and soil moisture flux to the atmosphere (9, 14, 15). At larger spatial scales, biophysical mechanisms operate through altered surface albedo and roughness, which decrease net radiation and atmospheric moisture convergence, thereby reducing rainfall (16, 17). When forest loss exceeds ~ 40% of a basin area, the breakdown of the vegetation–atmosphere feedback substantially diminishes regional precipitation and moisture recycling (18–20), delays the onset of the wet season in southern Amazonia (21, 22), and strengthens drought–deforestation feedback that propagate across the Andes–Amazon–Atlantic system (23). These processes reinforce each other, accelerating forest degradation and compromising the basin's resilience (17, 24). Under current deforestation trajectories, the region may experience up to a 10% reduction in rainfall and a 1–1.5°C rise in temperature by 2040 (25), potentially intensifying the duration and frequency of droughts. Business-as-Usual (BAU) projections for 2050 indicate rainfall decreases of 8–21% (18, 26), yet the downstream impacts of these hydrological changes on the western tropical North Atlantic (WTNA) remain largely unknown (9, 27).

The Amazon River contributes approximately 17% of the global freshwater discharge to the ocean (28, 29), sustaining one of the largest river plumes on Earth. This low-salinity lens, which can extend over 1–2 million km² and reach depths of 1–5 m (30–34), modulates the physical and chemical properties of the WTNA, influences regional circulation through buoyancy forcing, and affects air–sea exchanges of heat, water, and momentum (35–38). The plume dynamics result from the interplay among river discharge, wind forcing, tides, and the large-scale circulation of the North Brazil Current (NBC) and its retroflection into the North Equatorial Countercurrent (NECC), which regulates the formation and shedding of anticyclonic rings (32, 45). Through these mechanisms, the Amazon plume exerts a first-order control on stratification, barrier-layer formation, and the modulation of tropical Atlantic air–sea coupling (9, 32–34). However, despite the well-documented seasonal and interannual variability of the Amazon plume, its potential response to anthropogenic forcing, particularly deforestation-induced changes in continental freshwater exports, remains unexplored.

Deforestation-driven hydrological changes thus represent a missing link between continental land-use dynamics and tropical ocean circulation. Freshwater discharge anomalies can modify the salinity and temperature structure of the WTNA, influencing the strength of the NBC and NECC systems and altering barrier-layer thickness, vertical mixing, and latent-heat fluxes (9, 27, 38). Yet, existing studies have focused primarily on natural climate variability or idealized freshwater perturbations, without explicitly considering how land-use change alters the magnitude and timing of Amazon runoff.

Despite substantial advances in understanding the hydroclimatic impacts of Amazon deforestation and the variability of the Amazon River plume, the downstream consequences of land-use–driven hydrological change for tropical ocean circulation and upper-ocean heat exchange remain poorly quantified. Most previous studies have focused either on atmospheric and continental responses to deforestation or on oceanic variability under prescribed or idealized freshwater forcing, leaving a critical gap in understanding how projected forest loss may propagate through the river–plume–circulation continuum and reshape the physical state of the tropical Atlantic.

Here, we address this gap by allowing hydrological changes resulting from forest loss to be consistently transmitted from land to ocean using an offline combination of a hydrological and a regional ocean circulation model. We show how the business-as-usual deforestation projection for 2050, corresponding to approximately 45% forest loss, reduced freshwater export and modified surface salinity, the structure of the Amazon River plume, upper-ocean stratification, and surface heat exchange in the western tropical

North Atlantic. This study clarifies how land-use–driven hydrological change can reorganize tropical Atlantic circulation and heat distribution, establishing a mechanistic link between continental deforestation and ocean dynamics.

Results

Changes in river discharge induced by deforestation

The Amazon River discharge in the control experiment during DJF decreased by 30–50 % in the Madeira, Tapajós, and Xingu basins, with localized minima exceeding, 60 % near 10° S, 55° W(Figure 1c). Smaller reductions of 10–20 % extend across the central Amazon and lower Negro Basin. In MAM, negative anomalies expand northeastward into the Araguaia–Tocantins system and eastern Pará, where flow decreases by 20–40 % (Figure 1d). Central Amazonian tributaries remain within ±10 % of the control. Deficits intensify and cover most of the southern basin for JJA (Figure 1e). Broad regions with −40 % to −60 % anomalies stretch from Rondônia and Mato Grosso toward southern Pará, with localized minima below −60 % along the Tapajós headwaters and upper Xingu. Reduced discharge also extends westward toward the Madeira and Purus sub-basins. By SON (Figure 1f), runoff anomalies reach maximum spatial extent. A continuous band of −40 % to −60 % spans the southern uplands, lower Tocantins, and Maranhão coastal plain, while weaker positive differences (+10–20 %) remain limited to the upper Negro and western Solimões basins.

The net impact of deforestation in the ARB was assessed using the Óbidos station because it is considered the last hydrological station before the ocean, channeling about 90% of the total drainage in the basin (43,11). Deforestation-induced Amazon river flow reduction is more pronounced between May and November, reaching approximately a 12% decrease in September (Figure 2a). The long-term trend (1992 to 2015) the difference between the deforested and control scenarios, indicates that deforestation leading to a deforested area of ~45% by 2050 imposes a significant reduction in the total river flow discharged into the ocean ($p < 0.05$; Mann-Kendall trend test) (Figure 2d). A pronounced seasonal variability characterizes this long-term trend, with a significant positive discharge flow trend observed in JJA and a significant negative trend observed in SON, both exhibiting a magnitude of approximately 2% per decade ($p < 0.05$). In contrast, no statistically significant trend was discernible in DJF and MAM.

Surface Ocean Adjustments Induced by Changes in Amazon River Discharge

The impact of deforestation on SSS can be observed thousands of kilometres away from the river mouth (Figure 3). Deforestation leads to an increase in ocean salinity near the river mouth (~2 psu), especially during the JJA season. Conversely, positive SSS anomalies have been observed year-round along a wider expanse of the WTNA extending to 20°N, driven by northward boundary currents. Significant variations in SSS are predominantly observed westward of the river mouth and the NBCr river water export pathway. The magnitude of change between DJF and MAM is comparatively minimal (Figures 3a and 3b), as the reduced influence of the NBC allows the ARP to be confined along the coast by strong NE winds (44,45). Positive SSS anomalies start to build up along a narrow band in front of the river mouth since December.

It then spreads northwestwards with anomalies > 1 psu during MAM as far as the French Guyana, from where the salt tongue inflects towards the east with anomalies as high as 2 psu. This phenomenon occurs between JJA and SON, a time when the saltier ARP is captured by the NBCr and the NECC reaches full development.

Deforestation also induces marked seasonal and spatial variations in surface current anomalies across the western tropical Atlantic (Figure 4). For the zonal component (u), positive anomalies dominate most of the domain between 5° N and 12° N, with intensities ranging from 5 to 20 cm s^{-1} and peaks exceeding 25 cm s^{-1} near 8° N, 48° W during JJA and SON. Enhanced westward flow is observed along the North Brazil Current (NBC) pathway, while eastward anomalies develop along the 8–10° N band, consistent with stronger activity of the North Equatorial Countercurrent (NECC). In DJF and MAM, the u-component anomalies weaken, remaining confined to the offshore plume boundary between 50° W and 40° W, with magnitudes generally below 10 cm s^{-1}.

The meridional component (v) presents a zonally elongated wave-like pattern, alternating between positive and negative anomalies of ±10–15 cm s^{-1} aligned with the NBC and its retroflection (NBCr). Northward anomalies dominate between 8° N and 10° N, whereas southward anomalies prevail downstream of the retroflection, near 10° N, 52° W. The amplitude and spatial continuity of these alternating bands intensify from JJA to SON, coinciding with the period of maximum NBC transport and ring-shedding activity. Weaker and more fragmented anomalies are visible in DJF–MAM, mostly concentrated near 6–8° N.

The magnitude anomaly fields show two consistent zones of current acceleration. The first extends between 5° N and 10° N, 45–55° W, associated with the NBCr, where increases reach 10–14 cm s^{-1} during JJA–SON. The second lies north of 15° N, stretching toward the Antilles, where mean differences range from 6 to 10 cm s^{-1} across all seasons. In contrast, low-magnitude differences (< 4 cm s^{-1}) dominate the equatorial band and the inner shelf north of the Amazon mouth throughout the year. These patterns collectively depict a coherent seasonal reorganization of the near-surface flow, with stronger anomalies during boreal summer and autumn when mesoscale activity is at its peak.

Seasonal SST anomalies between the deforestation and control simulations display a distinct spatial structure across the western tropical North Atlantic, with alternating zones of warming and cooling that vary in position and intensity throughout the year (Figure 5).In DJF, negative anomalies dominate the coastal region from northern Brazil to French Guiana, forming a continuous cooling band between 2° N and 8° N, with magnitudes ranging from −0.2°C to −0.6°C. The strongest cooling is concentrated near the Amazon River mouth (50–52° W) and extends northeastward along the shelf toward 45° W. Offshore, weak positive anomalies (+0.1°C to +0.3°C) are scattered north of 10° N and east of 40° W, forming a broad, low-gradient warm sector in the central basin.

During MAM, SST anomalies weaken and lose zonal coherence. Small-scale warm patches (+0.2°C to +0.4°C) appear east of 35° W and between 5° N and 10° N, while residual cooling (−0.2°C to −0.4°C) persists along the Guianas shelf and in the near-equatorial region between 0° N and 5° N. The distribution becomes more irregular, with alternating bands of weak anomalies across the basin.

In JJA, contrasts intensify markedly. A broad coastal cooling pattern (−0.4°C to −0.6°C) develops along the northern Brazil and Guiana coasts, extending offshore to 48° W between 5° N and 10° N. In contrast, pronounced warming (+0.3°C to +0.5°C) emerges offshore north of 10° N, forming an elongated warm tongue that stretches from 50° W to 35° W, defining a sharp meridional gradient. Weaker anomalies (±0.2°C) are observed south of the equator and near 55° W.

By SON, SST anomalies shift toward overall warming. Positive values (+0.4°C to +0.6°C) dominate the area south of the Amazon mouth and extend northward along the Suriname and Guyana shelf. The warm region expands northeastward, linking with the offshore band around 10° N, 45° W, while residual cooling (−0.2°C to −0.3°C) persists near the equatorial zone east of 40° W. The seasonal transition from DJF to SON thus marks a progressive shift from coastal cooling to widespread offshore warming.

Overall, SST differences remain within −0.6°C to +0.6°C across the domain, with the strongest spatial gradients during JJA and SON, when warm and cold centers coexist within narrow latitudinal bands between 5° N and 12° N.

River outflow-driven changes in the vertical structure of the western Tropical Atalntic

Changes in MLD observed during the deforestation simulations have maximum amplitudes of ±8 m, developing mostly offshore between DJF and MAM (top maps in Fig. 6). These amplitudes become slightly lower around ±4 m between JJA and SON, but with a clear deepening of MLD along the coast following the NBCr and entering the NECC domain. The BLT, on the other hand, becomes up to 5 m shallower in this region during SON and DJF, but with the largest anomalies (±10 m) observed between MAM and JJA (middle maps in Figure 6). The latter shows a predominance of BLT shallowing northwest of the river mouth, close to the ring formation region (between 50° and 58°W and 5° to 10°N) and a thickening north of 10° N. Negative BLT anomalies become predominant again in SON but stronger than the observed in DJF. Latent heat fluxes are also altered by deforestation, reducing the latent heat flux to the atmosphere near the coast and in the northwest near the rings formation region. There is a clear transition in the spatial pattern of Latent heat Flux along the NBC and the GC domain with mostly positive (5 to 8 w/m2) anomalies in SON to negative (around -5 w/m2) in DJF (bottom maps in Figure 6).

Interannual and monthly changes in the Amazon River plume induced by deforestation

The time series of the simulated Amazon River Plume (ARP) area (Figure 7a) reveals a persistent and statistically significant long-term contraction over the 1992–2015 period. The Mann–Kendall test identifies a negative trend (Z = 2.28, p < 0.05), corresponding to a decline of approximately 23.4 × 10^3 km^2 per decade, or about 3% of the seasonal mean plume area. This long-term reduction is imposed on strong interannual variability, with alternating phases of expansion and contraction that reflect the hydrological response of the Amazon Basin. The amplitude of these fluctuations frequently exceeds ±400,000 km², highlighting the plume's sensitivity to continental discharge anomalies. The most pronounced reductions occurred in September 2005 and September 2010, when plume area decreased by over 600,000 km², coinciding with major El Niño–driven droughts that sharply curtailed river discharge. Conversely, transient expansions were observed in 1999, 2009, and 2013, corresponding to years of anomalously high Amazon flows during neutral or La Niña phases.

The mean seasonal cycle (Figure 7b) indicate that the ARP response to deforestation and hydroclimatic variability is not uniform throughout the year. From January to June, when the Amazon River experiences peak discharge, plume area anomalies remain smal, typically within - 5% of the climatological mean. Starting in July, negative anomalies intensify, reaching −10% to −15% in August–September and peaking at approximately −25% in November, coinciding with the end of the dry season and the minimum discharge period at Óbidos. This late-year contraction marks the period when the cumulative effects of reduced freshwater input and prolonged atmospheric drying most strongly limit plume spreading.

Discussion

Projected deforestation under the BAU-2050 scenario converts approximately 3.62×10^6 km² of forest to non-forest or deforested classes (Fig. 1a,b). The most extensive losses occur in Mato Grosso, Rondônia, Pará, and Maranhão, forming a contiguous arc from the Madeira and Tapajós headwaters through southern Pará to the Araguaia–Tocantins interfluve. Smaller, discontinuous patches appear in the upper Purus and Juruena sub-basins, while continuous forest remains in the central, northwestern, and western Amazon, particularly within the Negro and Solimões drainage systems. This redistribution of land cover reorganizes the Amazon basin's hydrological regime and transmits this perturbation to the Western Tropical North Atlantic (WTNA) through changes in buoyancy, salinity structure, and circulation. With ~ 45% forest loss, runoff declines sharply in the southern and eastern tributaries, where dry-season deficits exceed 50%, and discharge at Óbidos decreases by ~ 12% in September. These hydrological changes reduce the freshwater buoyancy input that sustains the Amazon River plume, leading to higher near-field surface salinity and steeper cross-shore gradients. Such steepening of horizontal salinity contrasts is consistent with classical plume theory (63, 65, 66), which predicts that reduced buoyancy flux compresses the frontal zone and confines the low-salinity lens closer to the coast. In our simulations, this adjustment manifests as a narrower and denser plume that remains coastal during DJF–MAM but becomes entrained into the North Brazil Current retroflection (NBCr) during JJA–SON, where positive salinity anomalies exceed + 1–2 PSU and extend northward along the NECC. This redistribution reflects the combined effect of weaker freshwater input and the stronger entrainment of the saltier surface layer into the NBC system.

The intensification of horizontal salinity gradients strengthens the NBC and Guiana Current by about 14%, particularly between 8° and 12°N, a region of frequent anticyclonic eddy formation (67, 68). Reduced freshwater buoyancy and thinning of the low-salinity lens weaken haline stratification, favoring stronger vertical shear and enhanced mesoscale variability. Although shear and stability were not explicitly quantified here, the displacement of the NBC retroflection and the strengthened mesoscale expression under reduced discharge are consistent with the baroclinic adjustments described in previous observational and modeling studies of the Amazon plume (32, 53, 69). These responses are most parsimoniously explained by an intensification of baroclinic-to-barotropic energy conversion as the buoyancy forcing weakens (66), amplifying the eddy field and modulating the transport of low-salinity waters toward the open ocean.

It is important to note that the atmospheric boundary conditions were identical over the ocean in both experiments. Continental precipitation, however, was adjusted following the empirical relationships of (18) to represent rainfall suppression under large-scale deforestation. The resulting anomalies therefore represent the downstream propagation of a land-surface perturbation, altered rainfall and runoff, under unchanged oceanic winds and heat fluxes. This setup isolates the hydrological component of deforestation, enabling the attribution of plume and circulation responses specifically to freshwater forcing rather than to coupled atmosphere–ocean feedback.

The reduction in Amazon discharge under the BAU-2050 scenario reflects the competing balance between two opposing mechanisms. At local scales, removal of forest cover reduces leaf area index, root depth, and surface roughness, lowering evapotranspiration and increasing the runoff coefficient (9, 14, 15). At basin scales exceeding the ~ 40% deforestation threshold, however, biophysical feedback dominate increased albedo, weaker moisture convergence, and reduced moisture recycling suppresses regional precipitation by 8–21% (18, 26). Climate–biosphere simulations have shown that this precipitation reduction outweighs the local evapotranspiration decrease, leading to net discharge reductions across most Amazon tributaries (19). By applying the Spracklen et al. (18) rainfall–deforestation relationships to the MGB precipitation forcing, our setup captures the dominant pathway of this large-scale feedback. The resulting Óbidos discharge decline, including the suppressed boreal-summer peak, therefore represents not an externally imposed drought but the downstream hydrological signature of vegetation–atmosphere feedbacks operating once forest loss surpasses the basin-scale non-linearity threshold (16, 73). The peak-flow attenuation in MAM–JJA reflects reduced accumulation during the preceding wet season, consistent with the delayed onset and weakened rainy season previously documented under high-deforestation scenarios (21, 22).

The vertical structure of the upper ocean adjusts coherently to the reduction in freshwater flux. The mixed layer deepens by up to ~ 8 m along the NBC and Guiana Current axis, while the barrier layer thickness (BLT) decreases by about 10 m, particularly over the ring-formation region. Observational estimates indicate that the Amazon plume sustains BLT values of 8–60 m (32); hence, the modeled reduction corresponds to a 40–60% weakening of haline stratification. The thinner barrier layer allows more efficient vertical mixing and entrainment of cooler subsurface waters, modifying the local heat budget despite identical atmospheric forcing. This explains the apparent sign reversals in latent heat flux (LHF), which become negative (–5 W m^{-2}) in DJF, when mixing-induced cooling suppresses upward heat flux near the coast, and positive (+ 5–8 W m^{-2}) in SON along the NBC/GC, where vertical exchange and SST recovery dominate. Similar behavior has been reported in coupled studies linking freshwater anomalies to enhanced vertical mixing and SST modulation in the WTNA (70). Therefore, even in the absence of direct atmospheric perturbations, the hydrological signal of deforestation reorganizes ocean stratification, mixing, and surface fluxes.

Sea-surface temperature (SST) anomalies mirror this interaction between mixing and advection. Cooling of up to − 0.45°C develops along the northern Brazilian shelf during DJF, collocated with maximum mixed-layer deepening and reduced LHF, whereas warm anomalies appear in SON south of the river mouth and along the NECC, where saltier waters are advected into the equatorial corridor. The 2–3-month lag between discharge minima (SON) and SST extrema (DJF) reflects the adjustment timescale of the upper ocean to Amazon freshwater forcing and is consistent with prior observations of Amazon–Atlantic coupling (11, 71, 72). This delayed response is consistent with a two-step adjustment process, involving an initial dynamical response of the plume and boundary currents to reduced freshwater input, followed by a more gradual thermodynamic adjustment associated with enhanced vertical mixing and surface heat fluxes. Over longer timescales, the simulations show a consistent contraction of the Amazon plume area (Mann–Kendall $Z = 2.28$, $p < 0.05$), decreasing by ≈ 23 × 10^3 km^2 per decade (~ 3% of the seasonal mean). The largest monthly reductions (~−25%) occur in November, coinciding with the seasonal discharge minimum, while interannual anomalies peak during the 2005 and 2010 droughts, years marked by suppressed basin-wide rainfall and warm North Atlantic SSTs (43). Given the strong correlation between plume area and Óbidos discharge ($r \approx 0.98$ monthly; $r \approx 0.58$ interannual) (47), even moderate hydrological perturbations lead to measurable shifts in the plume's spatial extent and stratification. This contraction reduces the WTNA's freshwater storage capacity and its buffering role in modulating salinity and temperature anomalies that influence ITCZ position and regional rainfall distribution (70).

Beyond these process-level results, this study provides a conceptual and methodological advance in the investigation of Amazon–Atlantic connectivity. Previous studies examined the seasonal and interannual variability of the plume under climate modes such as ENSO and the NAO, typically prescribing idealized river discharges (32, 40, 53). Here, the freshwater input originates from a hydrological model forced by a continental deforestation scenario, where rainfall and runoff anomalies are derived from rainfall–deforestation relationships (18). The resulting Amazon river outflow was fed into the ocean model as freshwater input boundary condition. This configuration represents a first attempt to simulate the propagation of a human-induced continental perturbation through the river–plume–current continuum. By linking changes in basin hydrology to the structure and variability of the WTNA, the results establish a mechanistic pathway relating land-use change to ocean dynamics, extending beyond descriptive plume climatologies and toward a process-based understanding of tropical ocean response to continental forcing.

Collectively, these results align with established theories of river-plume adjustment (65, 66) while extending them to an anthropogenic context. Reduced buoyancy steepens isopycnals at the shelf break and enhances frontal density gradients, strengthening the NBC and promoting more active eddy formation (68, 69). Concurrent BLT thinning, MLD deepening, and alternating LHF patterns explain the observed DJF cooling and SON warming. The amplified contraction of the ARP during drought years further suggests that externally imposed hydrological stressors intensify the natural variability of the system. The mechanisms identified here, (1) deforestation-induced reductions in rainfall and discharge of up to ~ 60% in tributaries and ~ 12% at Óbidos, (2) plume–circulation interaction steepening SSS fronts and strengthening NBC/NECC flow by ~ 14%, and (3) stratification–thermodynamic feedbacks leading to BLT thinning (~ 10 m), MLD deepening (~ 8 m), LHF reversals (–5 to + 8 W m^{-2}), and SST anomalies (–0.45°C to + 0.3°C), summarize how continental freshwater loss can reorganize the WTNA under unchanged atmospheric forcing.

Looking ahead, the mechanisms identified here outline a plausible trajectory for the Amazon–Atlantic system under continued forest loss. If deforestation surpasses the 40–50% threshold identified by hydrological projections (16, 73), the progressive reduction of freshwater export could shift the Amazon plume from a strongly stratified, seasonally pulsing feature to a more saline, dynamically thinner regime with reduced vertical stability. This transition would alter the balance between baroclinic and wind-driven processes along the NBC system (67, 68), deepen the mixed layer, and enhance air–sea heat exchange. A saltier and warmer surface layer could weaken regional convection and increase cross-equatorial SST gradients, displacing the ITCZ northward and feeding back on continental rainfall consistent with observed atmosphere–ocean feedback in the tropical Atlantic (74, 75). At the same time, a denser plume and modified stratification could influence Atlantic Niño development by altering the background thermocline structure and the west–east salinity contrast (70), with potential impacts on rainfall variability over Northeast Brazil and West Africa. These links suggest that the Amazon forest acts as a stabilizing element in the coupled Atlantic system, with its hydrological output regulating both the buoyancy-driven circulation of WTNA and the larger-scale climate gradients of the tropics. Future research should therefore expand this framework toward fully coupled Earth-system models and sustain observation of the Amazon plume using salinity, color, and velocity sensors. Integrating biogeochemical and ecological components into such models will also be critical to assess how altered plume dynamics may influence nutrient fluxes, productivity, and carbon exchange between the Amazon and the Atlantic. Understanding these cross-scale feedback will be essential to predict the resilience of the tropical Atlantic under simultaneous land-use change and climate warming.

This study focuses on the direct oceanic response to deforestation-driven changes in Amazon freshwater export by using prescribed atmospheric forcing in the ocean simulations. This experimental design allows the hydrological pathway linking continental forest loss to ocean circulation and heat distribution to be isolated and interpreted without confounding atmospheric variability. The resulting changes therefore represent robust modifications to the upper-ocean circulation and thermal structure that define the background state of the tropical Atlantic under sustained reductions in freshwater input. While atmosphere–ocean feedbacks may further modulate these responses under fully coupled conditions, the mechanisms identified here provide a physically grounded baseline for understanding how land-use change can precondition the tropical Atlantic ocean..

Data and Methods

Our Historical sensitivity study simulations were conducted using offline hidrological and oceanic simulations, combining the Great Basin Model (GBM) with the Regional Ocean Model System (ROMS), for the period 1992–2015. The impact of the business-as-usual scenario projected for 2050 on the Amazon on ocean variables in the Western Tropical North Atlantic was assessed.

Hydrological model

The MGB hydrological simulations for the Amazon River Basin (ARB) were configured following the methodology described by (57). Two land use and land cover scenarios were considered: (i) a historical baseline, based on Radambrasil (1982), Dijkshoorn et al. (2005), and Eva et al. (2002); and (ii) a Business-as-Usual (BAU-2050) scenario (following 56). Supplementary Figure S1a–b presents the land-use and land-cover classifications for both scenarios, while Supplementary Figure S1c–d shows the corresponding hydrological response units (HRUs) derived from 12,466 unit catchments.

The MGB model discretizes the basin into irregular grid cells using a digital elevation model (DEM). For this study, the 15-arcsecond HydroSHEDS DEM was employed, and all geoprocessing was performed using the IPH-Hydro Tools package (57). To represent the floodplain topography and drainage hierarchy, pits and depressions were removed through the Height Above the Nearest Drainage (HAND) method (58), which combines drainage directions from HydroSHEDS with the Bare-Earth SRTM v1 DEM. This configuration enables the model to capture the gradual transition between upland and floodplain areas, which is fundamental for accurately representing the low-slope hydrodynamics of the Amazon Basin.

The model was forced with meteorological variables including precipitation, air temperature, relative humidity, wind speed, atmospheric pressure, and solar irradiance. Precipitation forcing was obtained from the Multi-Source Weighted Ensemble Precipitation (MSWEP v1.1) dataset (59), and the remaining variables were derived from the Climate Research Unit (CRU) TS4.04 dataset. The simulation period spanned from 1990 to 2015, with the first year used for model spin-up and discarded from analysis.

In the BAU-2050 experiment, both land-use and land-cover maps and the precipitation field were modified to represent the combined effects of deforestation and its dominant atmospheric feedback on rainfall. Precipitation was adjusted at the sub-basin scale following the empirical relationships proposed in (18), which quantify wet- and dry-season rainfall reductions associated with forest loss and reproduce the spatial pattern of deforestation projected under the BAU-2050 scenario. These adjustments capture the primary hydrological consequences of deforestation, including changes in runoff driven by altered evapotranspiration, infiltration, and moisture recycling. Increased near-surface air temperature and reduced atmospheric humidity associated with deforestation were not explicitly prescribed in the simulations. However, observational and modeling studies indicate that these thermodynamic changes are largely mediated by, and strongly covary with, precipitation reductions at seasonal and regional scales (19, 20). By correcting precipitation consistently with deforestation-induced land–atmosphere feedbacks, the BAU-2050 setup therefore accounts indirectly for the dominant pathway through which deforestation modifies basin-scale hydrology. All remaining meteorological variables were kept identical across scenarios to isolate the hydrological signal of deforestation and to ensure that differences in runoff and freshwater export arise specifically from altered rainfall and land-cover forcing rather than from compounded atmospheric perturbations.

The MGB model computes daily runoff and streamflow using a distributed runoff–routing scheme that preserves the natural drainage network and the timing of tributary hydrographs. River discharge is calculated for major tributaries and aggregated at Óbidos to represent total freshwater export from the basin. Model performance was assessed using metrics such as the coefficient of determination (R^2) and root mean square error (RMSE) (Supplementary Fig s2).

Ocean Model

The Regional Ocean Modeling System (ROMS)(60) was used to simulate physical ocean processes in the Tropical North Atlantic Ocean. The model domain extended from 8°S to 22°N and 20°W to 60°W, with a horizontal resolution of 1/12° (~ 9 km in longitude). This resolution is sufficient to resolve the first radius of baroclinic Rossby deformation in the tropics (between 60 and 230 km)(61). This resolution is comparable to previous studies on ARP-related processes (32, 53, 54), making it suitable for resolving mesoscale features such as vortices and the retroflection of the North Brazil Current. A vertical grid with 40 sigma levels was utilized. Coastline data from the National Oceanic and Atmospheric Administration's (NOAA) World Coast Line (1:5,000,000 resolution) and bathymetry data from the ETOPO1 product (1 arc-minute resolution) were incorporated.

The model was forced by three primary components: river flow, atmospheric conditions, and tidal forcing. For the river flow forcing, the Óbidos flow was adopted, which in addition to having an adequate time series (from 1970 to the present) was used in several studies as the representative discharge of the Amazon River (27, 32, 53). Atmospheric forcing data, including precipitation rate, wind speed, surface air pressure, air temperature, relative humidity, solar shortwave radiation flux, and net longwave radiation flux, were derived from the Climate Forecast System Reanalysis (CFSR) and CFSR version 2 (CFSv2) datasets. Tidal forcing was incorporated using the TPXO9.1 product, which is crucial for accurately simulating plume mixing processes on the continental(62, 63, 64).

Initial and lateral boundary conditions were obtained from the Simple Ocean Data Assimilation (SODA) version 3.3.1 dataset. This dataset, generated by the Parallel Ocean Program (POP) general circulation model, provides three-dimensional variables (velocity, temperature, salinity) and two-dimensional variables (sea level height and vertically integrated velocity).

Following a two-year spin-up period to ensure dynamical equilibrium, the model outputs were validated against observational datasets: SST from the Operational Sea Surface Temperature and Sea Ice Analysis (OSTIA), SSS from the Soil Moisture and Ocean Salinity (SMOS) *satellite mission*, and surface current velocities from the Ocean Surface Current Analyses Real-time (OSCAR) product. To reconcile spatial resolution discrepancies, a bilinear interpolation scheme was applied. The model demonstrated robust performance, with results aligning closely with observational trends and agreeing with prior studies(32, 53, 65) Supplementary Fig. s3-6).

Estimation of the Mixed Layer Depth and Barrier Layer Thickness

The ocean mixed layer depth (MLD) and the barrier layer thickness (BLT) were calculated using the formalism presented by (27, 32). The MLD was determined using the density threshold (σ) method, meaning when an increase in σ occurs relative to a reference depth (near the surface):

$$\sigma_{t(z=CMO)} = \sigma_{t(\text{reference depth})} + \Delta\sigma_t \qquad (1)$$

Where σ is the potential density, and Δσ is the prescribed density increase. The reference depth was the shallowest layer of the ocean model outputs (between 0 and 1 meter).

The isothermal layer depth was calculated using the temperature difference equivalent to a 0.1 kg m^{-3} density increase from the reference depth, with salinity at the reference depth. The BLT is defined as the isothermal layer depth minus the MLD when the former is deeper than the latter, referred to as the compensation layer. Thus, only the BLT was analyzed.

Experiment Design

The experiment involved simulations using the MGB-IPH hydrological model (for the Amazon Basin) and the Roms model (for the WTNA). The deforestation scenario (Business-as-Usual for 2050) focused on its impacts on oceanic dynamics and thermodynamic processes. We applied precipitation corrections following(18) to account for land-atmosphere feedback under deforestation. The hydrological model was forced with 1990–2015 input data, and the resulting river discharges were used to force the ROMS ocean model.

We analyzed Runoff for the land and SSS, SST, surface currents (u,v) and magnitude, latent heat flux, mixed layer depth, and barrier layer thickness. Seasonal difference maps were computed across WTNA. The Amazon River Plume area considered was where SSS < 34.5 exists. A Mann-Kendall trend test (5% significance level) assessed whether land-use changes induced significant trends in continental freshwater discharge.

Declarations

Funding

Coordenação de Aperfeiçoamento de Pessoal de Nível Superior - Brasil (CAPES) - Finance Code 001.

Author Contribution

N.A.G. contributed to conceptualization, formal analysis, investigation, methodology, and writing – original draft; S.W. contributed to investigation, methodology, formal analysis, and review and editing; J.C.E. contributed to investigation, methodology, formal analysis, and review and editing; L.E.O.C.A.

contributed to investigation, formal analysis, and review and editing; E.T.P. contributed to investigation and review and editing; R.B.S. formal analysis; D.F.M.G. contributed to conceptualization, investigation, formal analysis, methodology, supervision, writing – original draft, and review and editing.

Acknowledgements

The authors acknowledge the institutions and data providers whose publicly available datasets supported the hydrological and oceanographic simulations conducted in this study. We thank the providers of HydroSHEDS and SRTM-derived elevation products used for basin discretization and hydrological preprocessing, as well as the developers of the IPH-Hydro Tools package. We also acknowledge the providers of MSWEP precipitation data and CRU climate data used to force the hydrological simulations. For the ocean simulations, we acknowledge the developers and maintainers of ROMS, the providers of CFSR/CFSv2 atmospheric forcing, TPXO tidal forcing, ETOPO1 bathymetry, NOAA coastline data, and SODA ocean reanalysis products used as initial and boundary conditions. We further acknowledge the OSTIA, SMOS, and OSCAR data products used for model evaluation. These datasets were essential for constructing, forcing, and validating the hydrological–ocean modeling framework used in this study. This study was financed in part by the Coordenação de Aperfeiçoamento de Pessoal de Nível Superior - Brasil (CAPES) - Finance Code 001.

Data Availability

The datasets used in this study include hydrodynamic model outputs and publicly available environmental datasets. The hydrodynamic model outputs generated during the present study are large-volume files and are therefore not deposited in a public repository. These data are available from the corresponding author upon reasonable request. The remaining datasets used as model forcing, boundary conditions, validation products, or ancillary data are publicly available and properly cited in the manuscript.

References

1. Arvor, D., Tritsch, I., Barcellos, C., Jégou, N. & Dubreuil, V. Land use sustainability on the South-Eastern Amazon agricultural frontier: Recent progress and the challenges ahead. *Appl. Geogr.* **80**, 86–97. https://doi.org/10.1016/j.apgeog.2017.02.009 (2017).
2. Spracklen, D. V. & Garcia-Carreras, L. The impact of Amazonian deforestation on Amazon basin rainfall. *Geophys. Res. Lett.* **42**, 9546–9552. https://doi.org/10.1002/2015GL066063 (2015).
3. DeFries, R. S., Rudel, T., Uriarte, M. & Hansen, M. Deforestation driven by urban population growth and agricultural trade in the twenty-first century. *Nat. Geosci.* **3**, 178–181. https://doi.org/10.1038/ngeo756 (2010).

4. Zalles, V. et al. Near doubling of Brazil's intensive row crop area since 2000. *Proc. Natl. Acad*. Sci. U.S.A. 116, 428–435, (2019). https://doi.org/10.1073/pnas.1810301115
5. Condé, T. M., Higuchi, N. & Lima, A. J. N. Illegal selective logging and forest fires in the Northern Brazilian Amazon. *Forests* 10, 61, (2019). https://doi.org/10.3390/f10010061
6. da Silva, C. F. A., de Andrade, M. O., dos Santos, A. M., Falcão, V. A. & Martins, S. F. The drivers of illegal mining on Indigenous Lands in the Brazilian Amazon. *Extract Ind. Soc.* **16**, 101354. https://doi.org/10.1016/j.exis.2023.101354 (2023).
7. Gibbs, H. K., Rausch, L., Munger, J., Schelly, I., Morton, D. C., Noojipady, P., …Walker, N. F. Brazil's soy moratorium. Science347, 377–378, DOI: https://doi.org/10.1126/science.aaa0181 (2015).
8. Gollnow, F., Cammelli, F., Carlson, K. M. & Garrett, R. D. Gaps in adoption and implementation limit the current and potential effectiveness of zero-deforestation supply chain policies for soy. *Environ. Res. Lett.* **17**, 114003. https://doi.org/10.1088/1748-9326/ac97f6 (2022).
9. Sierra, J. P. et al. Deforestation Impacts on Amazon-Andes Hydroclimatic Connectivity. *Clim. Dyn.* **58**, 2609–2637. https://doi.org/10.1007/s00382-021-06025-y (2022).
10. Ruiz-Vásquez, M., Arias, P. A., Martinez, J. A. & Espinoza, J. C. Effects of Amazon basin deforestation on regional atmospheric circulation and water vapor transport towards tropical South America. *Clim. Dyn.* **54**, 4169–4189. https://doi.org/10.1007/s00382-020-05223-4 (2020).
11. Gouveia, N. A., Gherardi, D. F. M. & Aragão, L. E. O. C. The role of the Amazon River plume on the intensification of the hydrological cycle. *Geophys. Res. Lett.* 46, 12221–12229, (2019). https://doi.org/10.1029/2019GL084302
12. Wongchuig, S. et al. Changes in the surface and atmospheric water budget due to projected Amazon deforestation: Lessons from a fully coupled model simulation. *J. Hydrol.* **625**, 130082. https://doi.org/10.1016/j.jhydrol.2023.130082 (2023).
13. Espinoza, J. C., Marengo, J. A., Schongart, J. & Jimenez, J. C. The new historical flood of 2021 in the Amazon River compared to major floods of the 21st century: Atmospheric features in the context of the intensification of floods. *Weather Clim. Extrem*. **35**, 100406. https://doi.org/10.1016/j.wace.2021.100406 (2022).
14. Aragão, L. E. O. C. The rainforest’s water pump. *Nature* **489**, 217–218. https://doi.org/10.1038/489217a (2012).
15. Müller, R., Müller, D., Schierhorn, F., Gerold, G. & Pacheco, P. Proximate causes of deforestation in the Bolivian lowlands: An analysis of spatial dynamics. *Reg. Environ. Change*. **12**, 445–459. https://doi.org/10.1007/s10113-011-0259-1 (2011).
16. Zemp, D. et al. Self-amplified Amazon forest loss due to vegetation-atmosphere feedbacks. *Nat. Commun.* **8**, 14681. https://doi.org/10.1038/ncomms14681 (2017).
17. Staal, A. et al. Forest-rainfall cascades buffer against drought across the Amazon. *Nat. Clim. Change*. **8**, 539–543. https://doi.org/10.1038/s41558-018-0177-y (2018).
18. Spracklen, D. V., Arnold, S. R. & Taylor, C. Observations of increased tropical rainfall preceded by air passage over forests. *Nature* **489**, 282. https://doi.org/10.1038/nature11390 (2012).

19. Coe, M. T., Costa, M. H. & Soares-Filho, B. S. The influence of historical and potential future deforestation on the stream flow of the Amazon River – Land surface processes and atmospheric feedbacks. *J. Hydrol.* **369**, 165–174. https://doi.org/10.1016/j.jhydrol.2009.02.043 (2009).
20. Senna, M. C. A., Costa, M. H. & Pires, G. F. Vegetation-atmosphere-soil nutrient feedbacks in the Amazon for different deforestation scenarios. *J. Geophys. Res. Atmos.* **114**, D4. https://doi.org/10.1029/2008JD010401 (2009).
21. Commar, L. F. S., Abrahão, G. M. & Costa, M. H. A possible deforestation-induced synoptic-scale circulation that delays the rainy season onset in Amazonia. *Environ. Res. Lett.* **18**, 044041. https://doi.org/10.1088/1748-9326/acc95f (2023).
22. Sierra, J. P. et al. Impacts of land-surface heterogeneities and Amazonian deforestation on the wet season onset in southern Amazon. *Clim. Dyn.* **61**, 4867–4898. https://doi.org/10.1007/s00382-023-06835-2 (2023).
23. Beveridge, C. F., Espinoza, J. C., Athayde, S., Correa, S. B., Couto, T. B., Heilpern,S. A., … Anderson, E. P. The Andes–Amazon–Atlantic pathway: A foundational hydroclimate system for social–ecological system sustainability. Proc. Natl. Acad. Sci. U.S.A.121, e2306229121, DOI: https://doi.org/10.1073/pnas.2306229121 (2024).
24. Lapola, D. M., Silva, J. M. C. D., Braga, D. R., Carpigiani, L., Ogawa, F., Torres,R. R., … Joly, C. A. A climate-change vulnerability and adaptation assessment for Brazil's protected areas. Conserv. Biol.34, 427–437, DOI: https://doi.org/10.1111/cobi.13405 (2020).
25. Ferreira, F. L. V., Silva, A. A., Santos, V. J. & Calijuri, M. L. Deforestation in the Legal Amazon: The impacts of human action on the regional climate scenario. *Preprint* (2021). https://doi.org/10.21203/rs.3.rs-669277/v1
26. Spracklen, D. V. & Garcia-Carreras, L. The impact of Amazonian deforestation on Amazon basin rainfall. *Geophys. Res. Lett.* **42**, 9546–9552. https://doi.org/10.1002/2015GL066063 (2015).
27. Liang, Y. C. et al. Amplified seasonal cycle in hydroclimate over the Amazon River basin and its plume region. *Nat. Commun.* **11**, 4390. https://doi.org/10.1038/s41467-020-18187-0 (2020).
28. Goes, J. I. et al. do„, Influence of the Amazon River discharge on the biogeography of phytoplankton communities in the western tropical north Atlantic. *Prog. Oceanogr.* 120, 29–40, (2014). https://doi.org/10.1016/j.pocean.2013.07.010
29. Giffard, P., Llovel, W., Jouanno, J., Morvan, G. & Decharme, B. Contribution of the Amazon River discharge to regional sea level in the tropical Atlantic Ocean. *Water* **11**, 2348. https://doi.org/10.3390/w11112348 (2019).
30. Ibánhez, J. S. P., Diverrès, D., Araujo, M. & Lefèvre, N. Seasonal and interannual variability of sea-air CO_2 fluxes in the tropical Atlantic affected by the Amazon River plume. *Global Biogeochem. Cycles*. **29**, 1640–1655. https://doi.org/10.1002/2015GB005110 (2015).
31. Lefèvre, N. et al. S. P. Net heterotrophy in the Amazon continental shelf changes rapidly to a sink of CO_2 in the outer Amazon plume. *Front. Mar. Sci.* **4**, 278. https://doi.org/10.3389/fmars.2017.00278 (2017).

32. Varona, H., Veleda, D., Silva, M., Cintra, M. & Araujo, M. Amazon river plume influence on western tropical Atlantic dynamic variability. *Dyn. Atmos. Oceans*. **85**, 1–15. https://doi.org/10.1016/j.dynatmoce.2018.12.001 (2019).

33. Vizy, E. K. & Cook, K. H. Influence of the Amazon/Orinoco plume on the summertime Atlantic climate. *J. Geophys. Res. Atmos.* **115**, D21112. https://doi.org/10.1029/2010JD014049 (2010).

34. Jahfer, S., Vinayachandran, P. & Nanjundiah, R. S. Long-term impact of Amazon River runoff on northern hemispheric climate. *Sci. Rep.* **7**, 10989. https://doi.org/10.1038/s41598-017-10750-y (2017).

35. Medeiros, P. M. et al. Fate of the Amazon River dissolved organic matter in the tropical Atlantic Ocean. *Global Biogeochem. Cycles*. **29**, 677–690. https://doi.org/10.1002/2015GB005115 (2015).

36. Satinsky, B. M. et al. Expression patterns of elemental cycling genes in the Amazon River Plume. *ISME J.* 11, 1852–1864, (2017). https://doi.org/10.1038/ismej.2017.46

37. Gouveia, N. A. et al. O. C. The salinity structure of the Amazon River plume drives spatiotemporal variation of oceanic primary productivity. *J. Geophys. Res. Biogeosci.* 124, 147–165, (2019). https://doi.org/10.1029/2018JG004665

38. Rudzin, J. E., Shay, L. K. & de la Jaimes, B. The impact of the Amazon-Orinoco River plume on enthalpy flux and air-sea interaction within Caribbean Sea tropical cyclones. *Mon Weather Rev.* **147**, 931–950. https://doi.org/10.1175/MWR-D-18-0348.1 (2019).

39. Gloor, M. et al. Recent Amazon climate as background for possible ongoing and future changes of Amazon humid forests. *Global Biogeochem. Cycles* 29, 1384–1399, (2015). https://doi.org/10.1002/2014GB005080

40. Hu, C., Montgomery, E. T., Schmitt, R. W. & Muller-Karger, F. E. The dispersal of the Amazon and Orinoco River water in the tropical Atlantic and Caribbean Sea: Observation from space and S-PALACE floats. *Deep-Sea Res. Pt II*. **51**, 1151–1171. https://doi.org/10.1016/j.dsr2.2004.04.001 (2004).

41. Jahfer, S., Vinayachandran, P. N. & Nanjundiah, R. S. The role of Amazon River runoff on the multidecadal variability of Atlantic ITCZ. *Environ. Res. Lett.* **15**, 054013. https://doi.org/10.1088/1748-9326/ab7a6e (2020).

42. Soares-Filho, B. S. et al. Modeled deforestation scenarios, Amazon Basin, 2002–2050. ORNL DAAC, (2013). https://doi.org/10.3334/ORNLDAAC/1153

43. Zeng, N. et al. Causes and impacts of the 2005 Amazon drought. *Environ. Res. Lett.* **3**, 014002. https://doi.org/10.1088/1748-9326/3/1/014002 (2008).

44. Stramma, L. & Schott, F. The mean flow field of the tropical Atlantic Ocean. *Deep Sea Res. Part. II Top. Stud. Oceanogr.* **46**, 279–303. https://doi.org/10.1016/S0967-0645(98)00109-X (1999).

45. Johns, W. E., Townsend, T. L., Fratantoni, D. M. & Wilson, W. D. On the Atlantic inflow to the Caribbean Sea. *Deep Sea Res. Part. I Oceanogr. Res. Pap*. **49**, 211–243. https://doi.org/10.1016/S0967-0637(01)00041-3 (2002).

46. Marengo, J. A. & Espinoza, J. C. Extreme seasonal droughts and floods in Amazonia: Causes, trends and impacts. *Int. J. Climatol.* **36** (3), 1033–1050. https://doi.org/10.1002/joc.4420 (2016).

47. Molleri, G. S., Novo, E. M. D. M. & Kampel, M. Space-time variability of the Amazon River plume based on satellite ocean color. *Cont. Shelf Res.* **30** (3–4), 342–352. https://doi.org/10.1016/j.csr.2009.11.015 (2010).

48. Espinoza, J. C., Ronchail, J., Marengo, J. A. & Segura, H. Contrasting north–south changes in Amazon wet-day and dry-day frequency and related atmospheric features (1981–2017). *Clim. Dyn.* **52**, 5413–5430. https://doi.org/10.1007/s00382-018-4462-2 (2018).

49. Boers, N., Marwan, N., Barbosa, H. M. & Kurths, J. A deforestation-induced tipping point for the South American monsoon system. *Sci. Rep.* **7**, 41489. https://doi.org/10.1038/srep41489 (2017).

50. Pires, G. F. & Costa, M. H. Deforestation causes different subregional effects on the Amazon bioclimatic equilibrium. *Geophys. Res. Lett.* **40**, 3618–3623. https://doi.org/10.1002/grl.50570 (2013).

51. Sampaio, G. et al. Regional climate change over eastern Amazonia caused by pasture and soybean cropland expansion. *Geophys. Res. Lett.* **34**, L17709. https://doi.org/10.1029/2007GL030612 (2007).

52. Huang, B. & Mehta, V. M. Influences of freshwater from major rivers on global ocean circulation and temperatures in the MIT ocean general circulation model. *Adv. Atmos. Sci.* **27**, 455–468. https://doi.org/10.1007/s00376-009-9022-6 (2010).

53. Coles, V. J. et al. The pathways and properties of the Amazon River plume in the tropical North Atlantic Ocean. *J. Geophys. Research: Oceans*. **118**, 6894–6913. https://doi.org/10.1002/jgrc.20280 (2013).

54. Masson, S. & Delecluse, P. Influence of the Amazon River runoff on the tropical Atlantic. *Phys. Chem. Earth Part B*. **26**, 137–142. https://doi.org/10.1016/S1464-1909(00)00228-2 (2001).

55. Aragão, L. E. O. C. et al. Interactions between rainfall, deforestation and fires during recent years in the Brazilian Amazonia. *Geophys. Res. Lett.* **34** (17), L17701. https://doi.org/10.1029/2007GL030575 (2007).

56. Soares-Filho, B. S. et al. LBA-ECO LC-14 Modeled Deforestation Scenarios: Amazon Basin, 2002–2050, (2013). https://doi.org/10.3334/ORNLDAAC/1153

57. Siqueira, V. A. et al. Toward continental hydrologic-hydrodynamic modeling in South America. *Hydrol. Earth Syst. Sci.* **22**, 4815–4842. https://doi.org/10.5194/hess-22-4815-2018 (2018).

58. Rennó, C. D. et al. HAND, a new terrain descriptor using SRTM-DEM: Mapping terra-firme rainforest environments in Amazonia. *Remote Sens. Environ.* **112**, 3469–3481. https://doi.org/10.1016/j.rse.2008.08.009 (2008).

59. Beck, H. E. et al. 3-hourly 0.25° global gridded precipitation (1979–2015) by merging gauge, satellite, and reanalysis data. *Hydrol. Earth Syst. Sci.* **21**, 589–615. https://doi.org/10.5194/hess-21-589-2017 (2017).

60. Shchepetkin, A. F. & McWilliams, J. C. The regional oceanic modeling system (ROMS): A split-explicit, free-surface, topography-following-coordinate oceanic model. *Ocean Model.* **9**, 347–404.

https://doi.org/10.1016/j.ocemod.2004.08.002 (2005).

61. Chelton, D. B., Deszoeke, R. A., Schlax, M. G., Naggar, K. E. & Siwertz, N. Geographical variability of the first baroclinic Rossby radius of deformation. *J. Phys. Oceanogr.* **28**, 433–460. https://doi.org/10.1175/1520-0485(1998)028%3C0433:GVOTFB%3E2.0.CO;2 (1998).
62. Beardsley, R. C. et al. The M2 tide on the Amazon shelf. *J. Geophys. Research: Oceans*. **100**, 2283–2319. https://doi.org/10.1029/94JC01688 (1995).
63. Lentz, S. J. & Limeburner, R. The Amazon River plume during AMASSEDS: Subtidal current variability and the importance of wind forcing. *J. Phys. Res.* **100**, 2377–2390. https://doi.org/10.1029/94JC00343 (1995).
64. Niklema, O., Devenon, J. L. & Baklouti, M. Numerical modeling of the Amazon River plume. *Cont. Shelf Res.* **27**, 873–899. https://doi.org/10.1016/j.csr.2007.01.001 (2007).
65. Garvine, R. W. A dynamical system for classifying buoyant coastal discharges. *Cont. Shelf Res.* **15**, 1585–1596. https://doi.org/10.1016/0278-4343(95)00026-7 (1995).
66. Fong, D. A. & Geyer, W. R. The alongshore transport of freshwater in a surface-trapped river plume. *J. Phys. Oceanogr.* **32**, 957–972. https://doi.org/10.1175/1520-0485(2002)032 (2002).
67. Johns, W. E. et al. Annual cycle and variability of the North Brazil Current. *J. Phys. Oceanogr.* **28**, 103–128. https://doi.org/10.1175/1520-0485(1998)028 (1998).
68. Fratantoni, D. M. & Glickson, D. A. North Brazil Current ring generation and evolution observed with SeaWiFS. *J. Phys. Oceanogr.* **32**, 1058–1074. https://doi.org/10.1175/1520-0485(2002)032 (2002).
69. Grodsky, S. A., Reverdin, G., Carton, J. A. & Coles, V. J. Year-to-year salinity changes in the Amazon plume region. *Geophys. Res. Lett.* **41**, 548–554. https://doi.org/10.1002/2013GL058665 (2014).
70. Foltz, G. R. et al. The tropical Atlantic observing system. *Front. Mar. Sci.* **6**, 206. https://doi.org/10.3389/fmars.2019.00206 (2019).
71. Hellweger, F. L. & Gordon, A. L. Tracing Amazon River water into the Caribbean Sea. *J. Mar. Res.* **60**, 537–549. https://doi.org/10.1357/002224002321505102 (2002).
72. Balaguru, K., Chang, P., Saravanan, R. & Jang, C. J.The barrier layer of the Atlantic warm pool: Formation mechanism and influence on the mean climate. *Tellus A*. **64**, 18162. https://doi.org/10.3402/tellusa.v64i0.18162 (2012).
73. Lovejoy, T. E. & Nobre, C. Amazon tipping point. *Sci. Adv.* **4**, eaat2340. https://doi.org/10.1126/sciadv.aat2340 (2018).
74. Xie, S. P. & Carton, J. A. Tropical Atlantic variability: Patterns, mechanisms, and impacts. Earth's Climate: The Ocean–Atmosphere Interaction (AGU Geophysical Monograph Series) 147, 121–142. (2004). https://doi.org/10.1029/147GM07
75. Biasutti, M., Sobel, A. H. & Kushnir, Y. AGCM precipitation biases in the tropical Atlantic. *J. Clim.* **25**, 935–958. https://doi.org/10.1175/JCLI-D-11-00107.1 (2012).

Figures

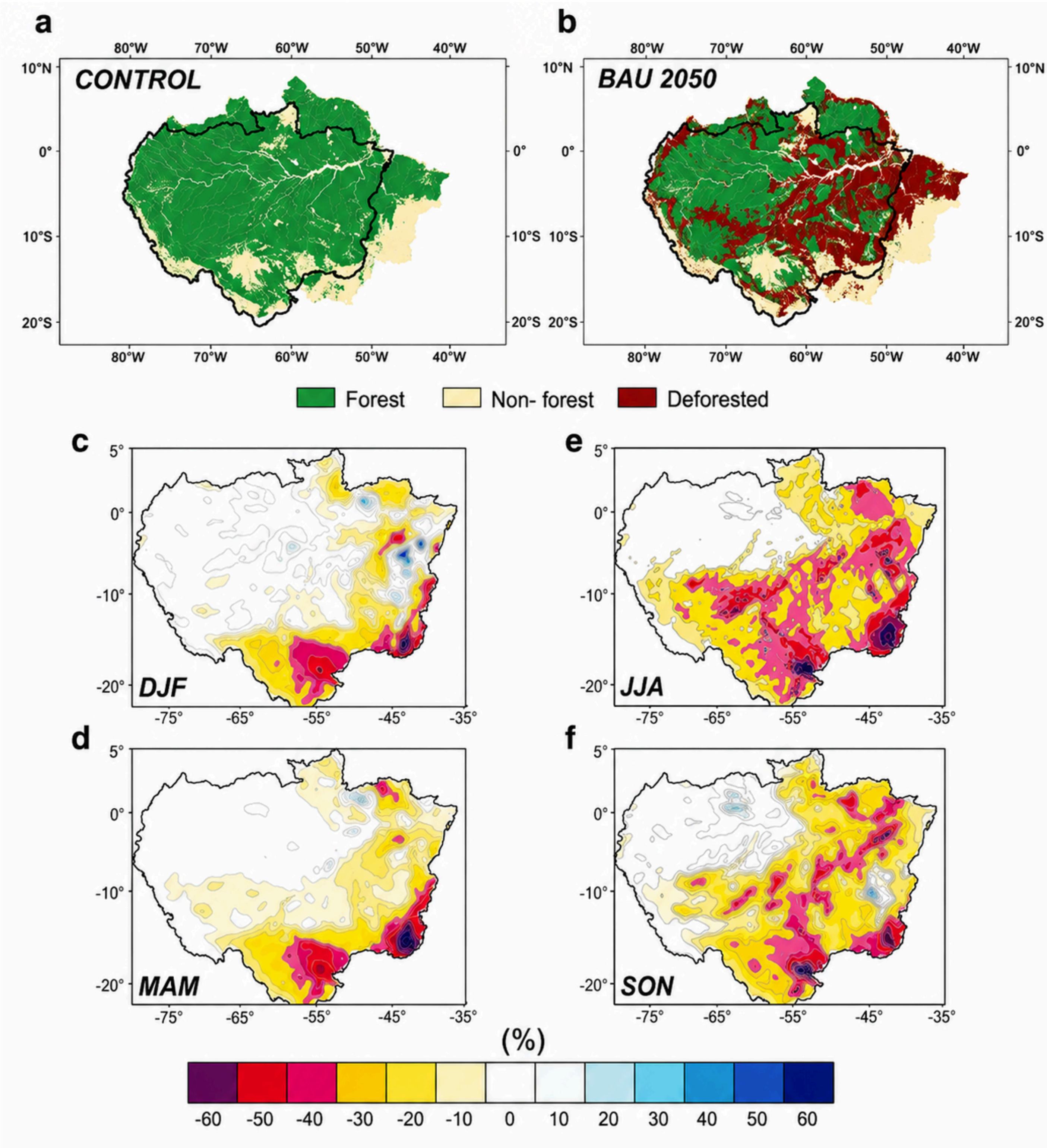

Figure 1

Seasonal composites (1992-2015) of differences between flow scenarios (deforested - control)

aLand cover fraction maps (2010) for forest and non-forest (control scenario). **b**Projected land cover for 2050 under deforestation following the LC-14 business-as-usual scenario (42). Seasonal composites

(1992–2015) of differences (deforested – control) across all hydrological response units (see methods) for DJF **c**, MAM d, JJA **e**, and SON **f**. The black outline denotes the Amazon River basin boundary.

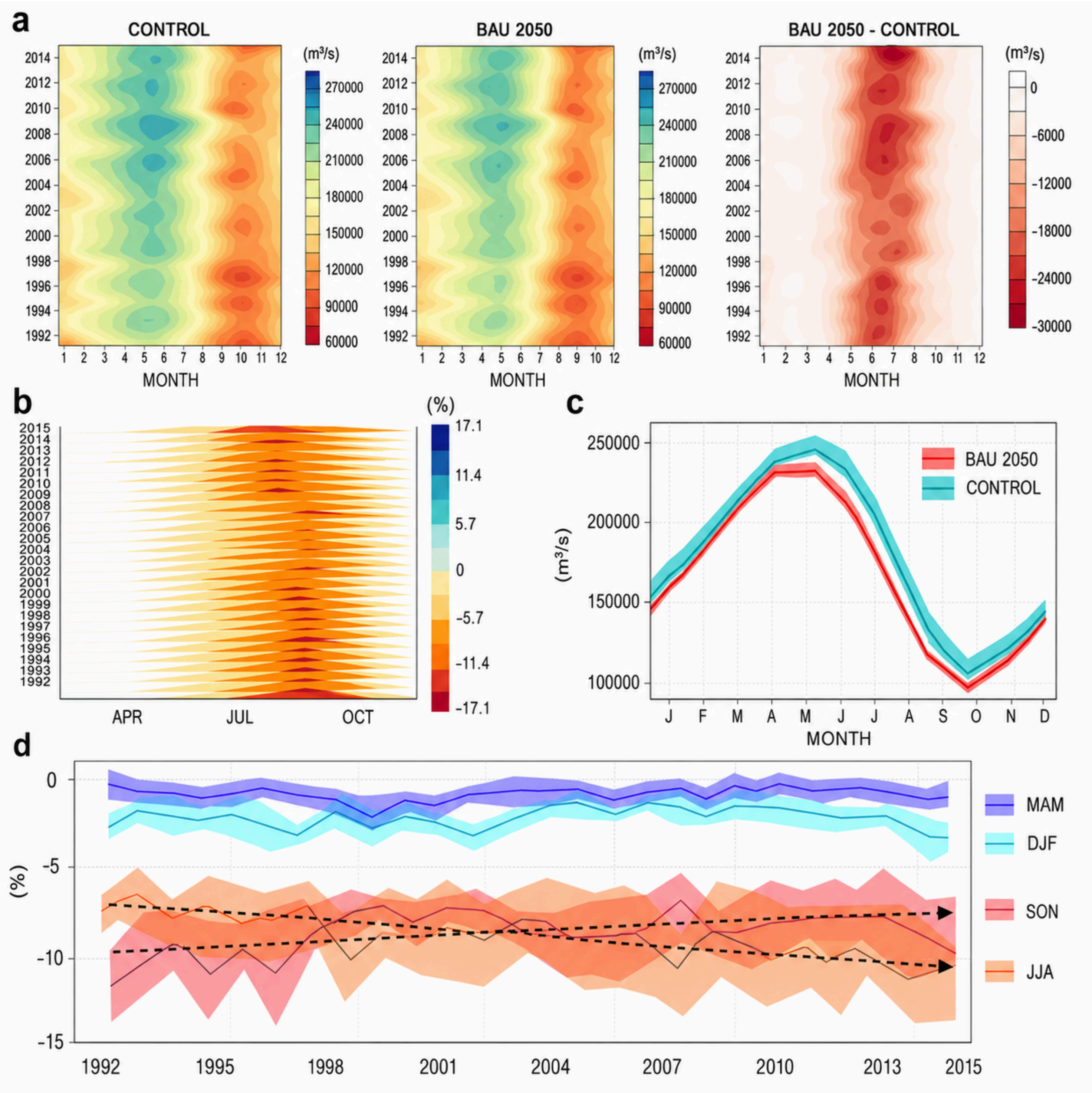

Figure 2

Seasonal and interannual variability of Óbidos River flow

aEvolution of the Óbidos flow from 1992 to 2015 (two panels on the left) and the difference between them (panel on the right). **b** evolution of the percentage difference in Óbidos flows over years and months. **c** Monthly climatology of the Óbidos flow. **d** temporal analysis of the relative differences by season (DJF, MAM, JJA, SON). The shadows in the graphs represent the standard deviation, while the dashed line in figure **d** represents significant trends (Mann-Kendall, p<0.05).

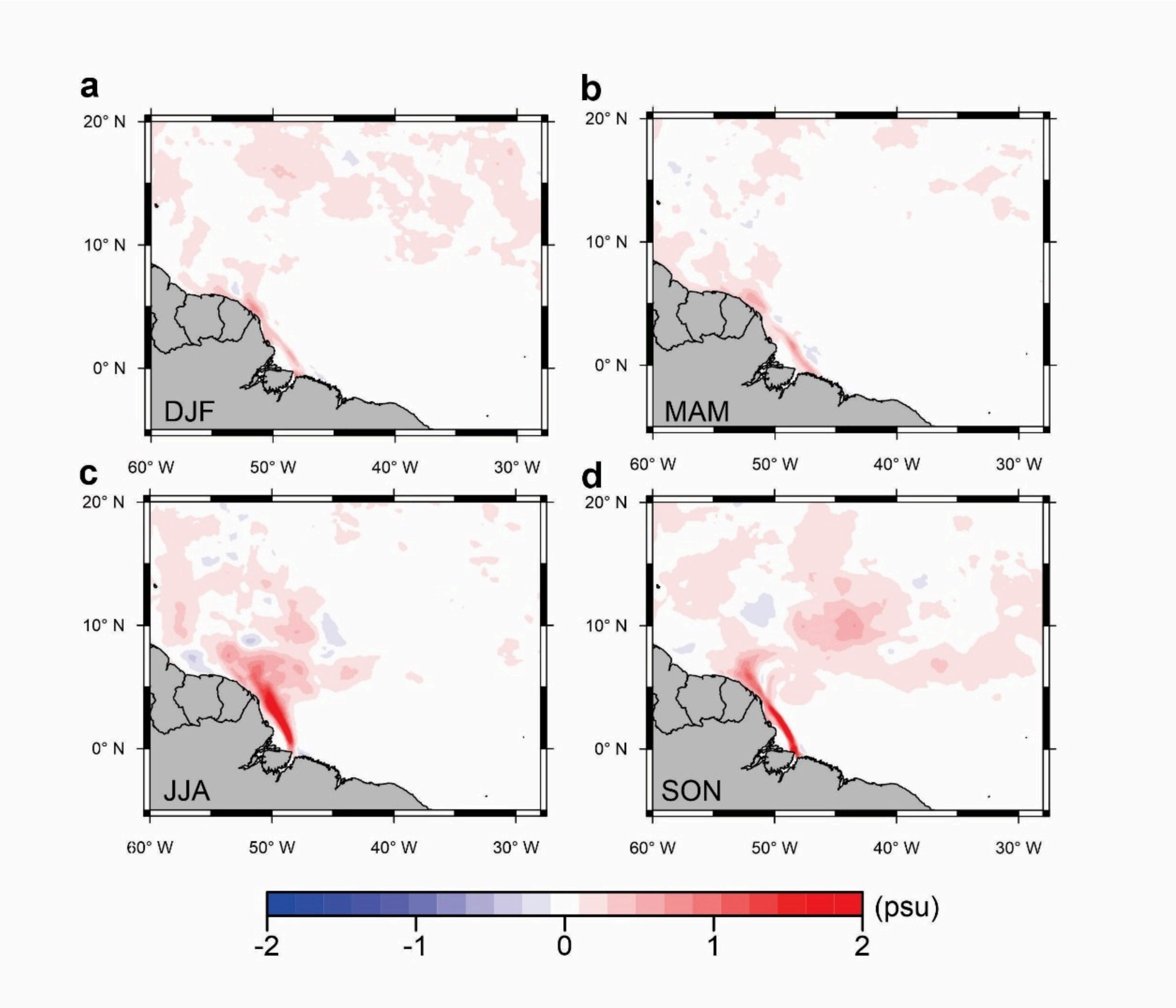

Figure 3

Seasonal Sea Surface Salinity (SSS) Differences Between Deforestation and Control Simulations

Maps depicting mean seasonal differences in SSS (psu) between simulations (deforestation minus control) from 1992 to 2015) for **a** DJF, **b** MAM, **c** JJA and **d** SON.

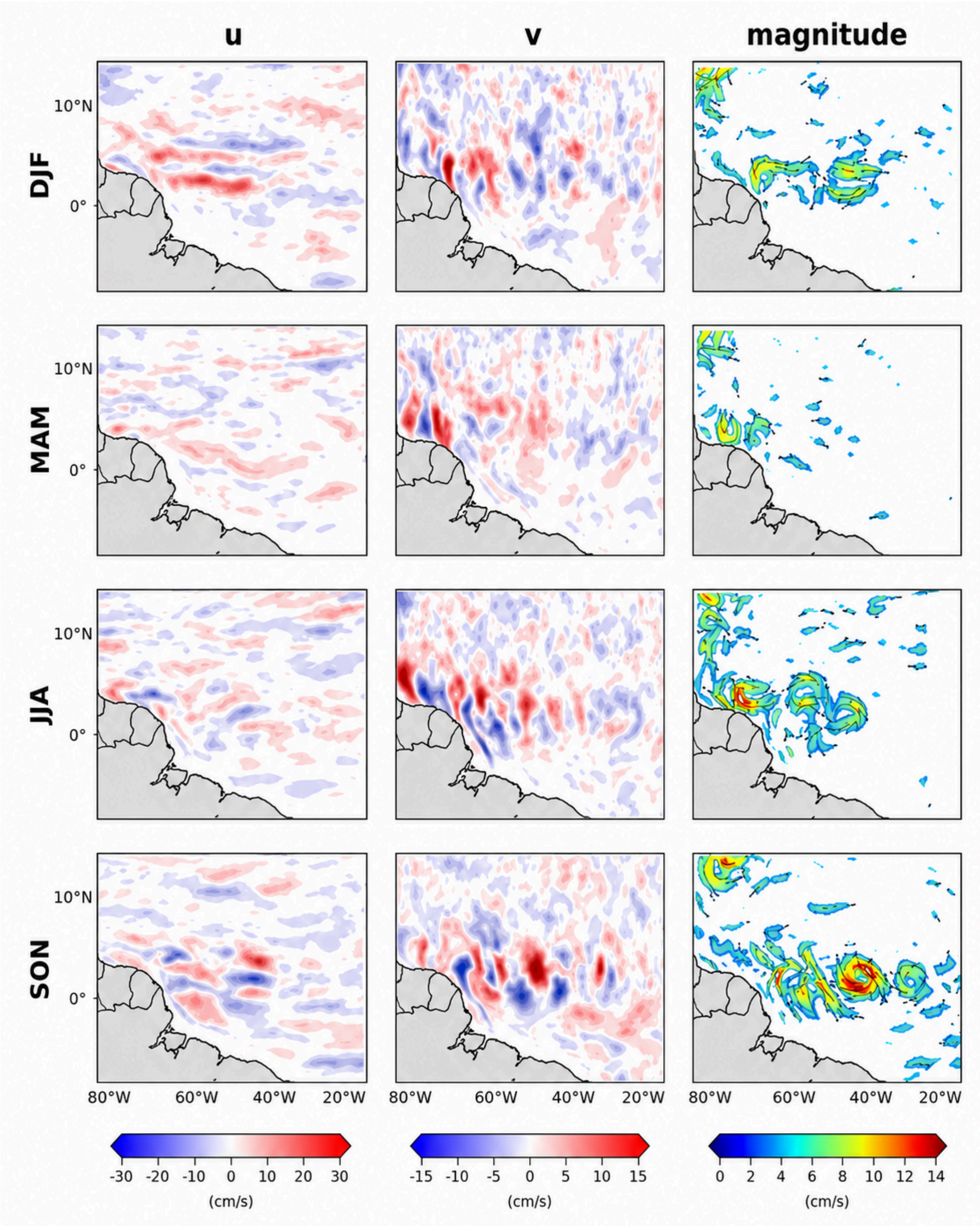

Figure 4

Maps depicting mean seasonal differences(deforestation minus control) for the magnitude, zonal and meridional surface current velocity (cms −1) from 1992 to 2015.

In each panel, the column represent zonal velocity (first), meridional velocity (second), and velocity magnitude (tird). The rows correspond to different stations: the first for DJF (December–February), the second for MAM (March–May), the third for JJA (June–August), and the fourth for SON (September–November). The length of the vectors indicates the magnitude of surface velocity differences, while their direction shows the orientation of the change.

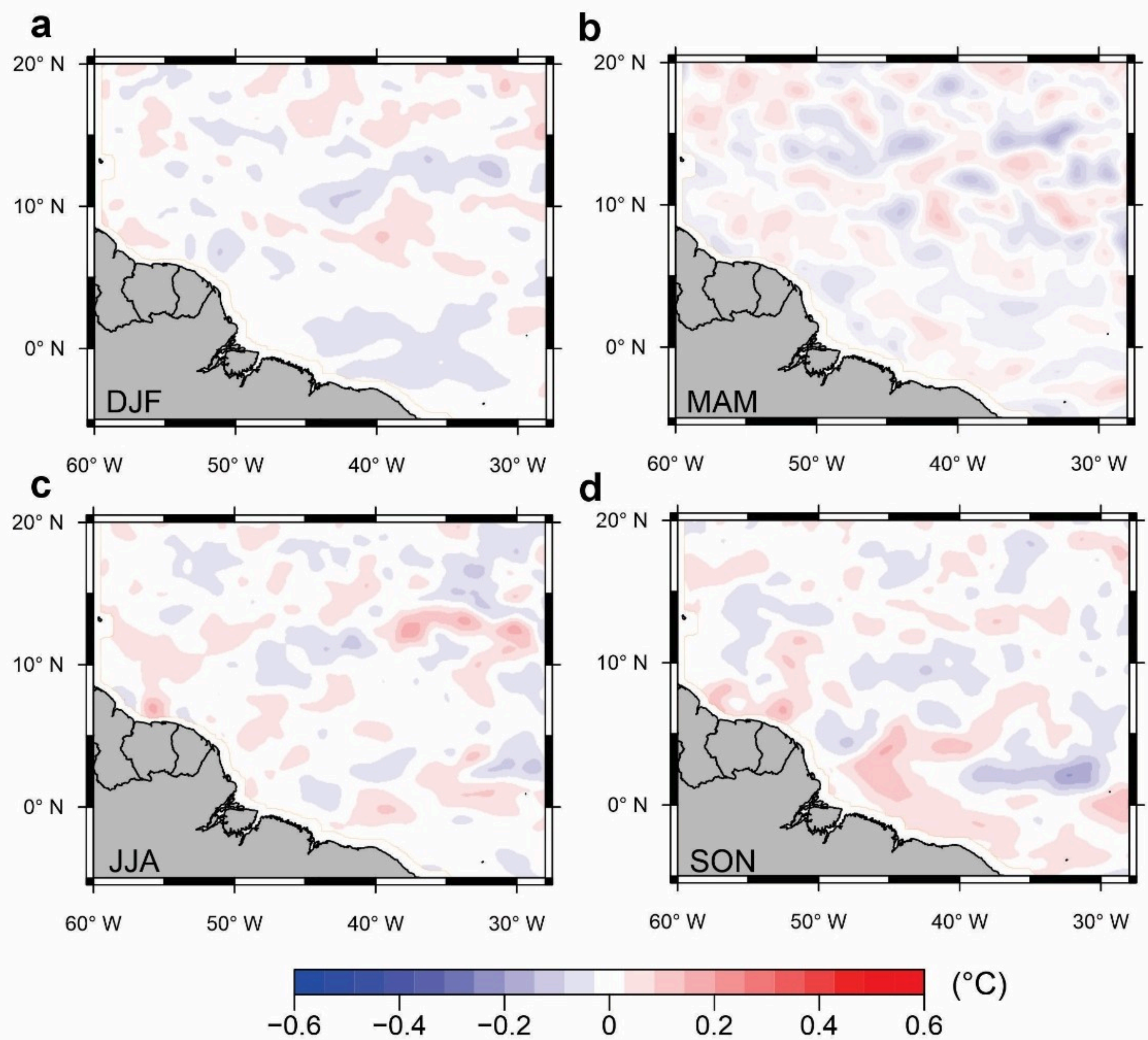

Figure 5

Seasonal Sea Surface Temperature (SST) Differences Between Deforestation and Control Simulations

Maps depicting mean seasonal differences in SST(°C) between simulations (deforestation minus control) from 1992 to 2015) for **a** DJF, **b** MAM, **c** JJA and **d** SON.

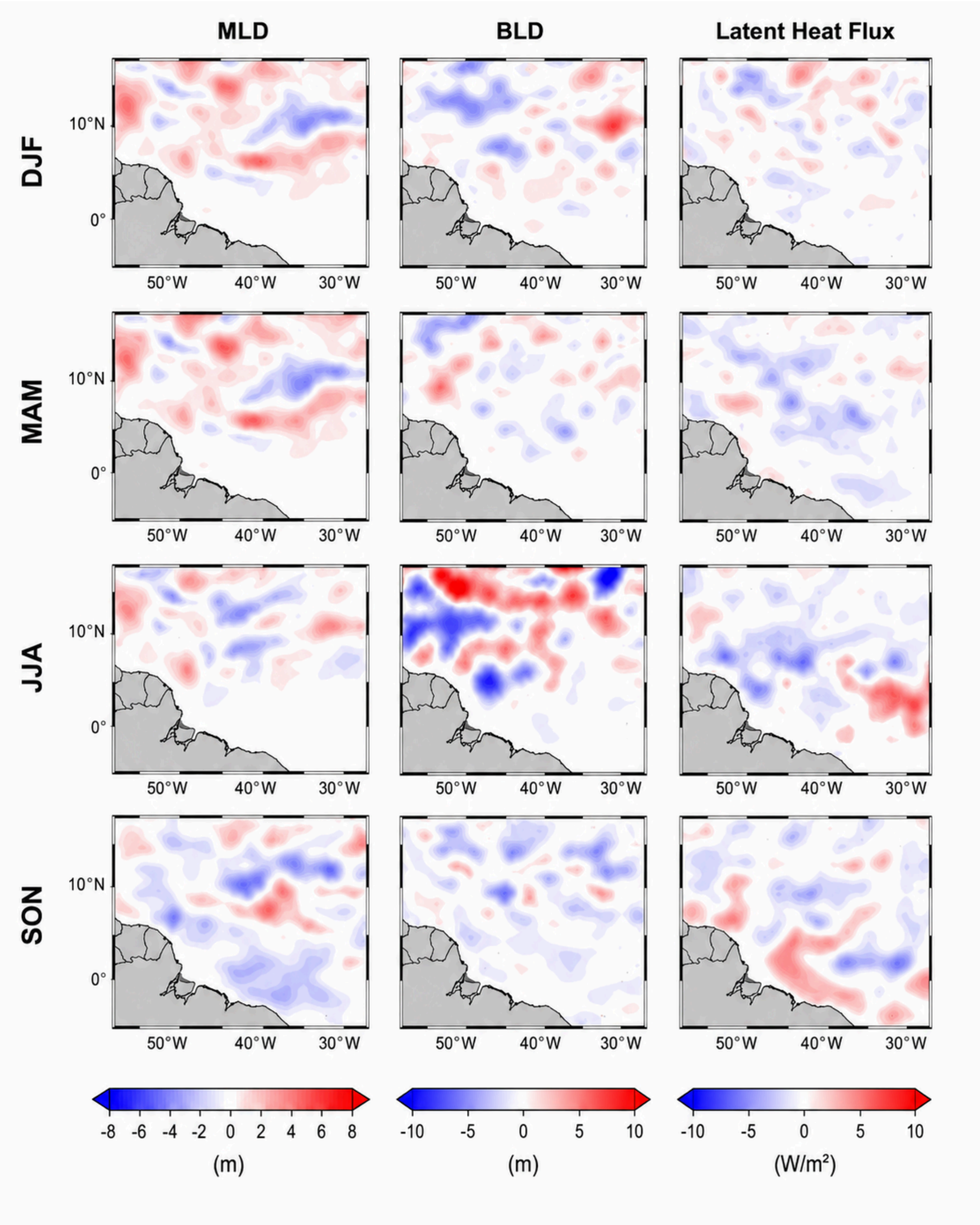

Figure 6

Seasonal differences between the deforested and control scenarios (1992–2015) are shown for mixed layer depth (MLD), barrier layer thickness (BLT), and latent heat flux

Each panel shows the seasonal differences between the deforested and control scenarios over the period 1992–2015. The columns represent different variables: mixed layer depth (MLD) in the first, barrier layer thickness (BLT) in the second, and latent heat flux in the tird. The rows represent the four climatological seasons: DJF (December–February), MAM (March–May), JJA (June–August), and SON (September–November). Positive values indicate higher values in the deforested scenario compared to the control, and negative values indicate the opposite.

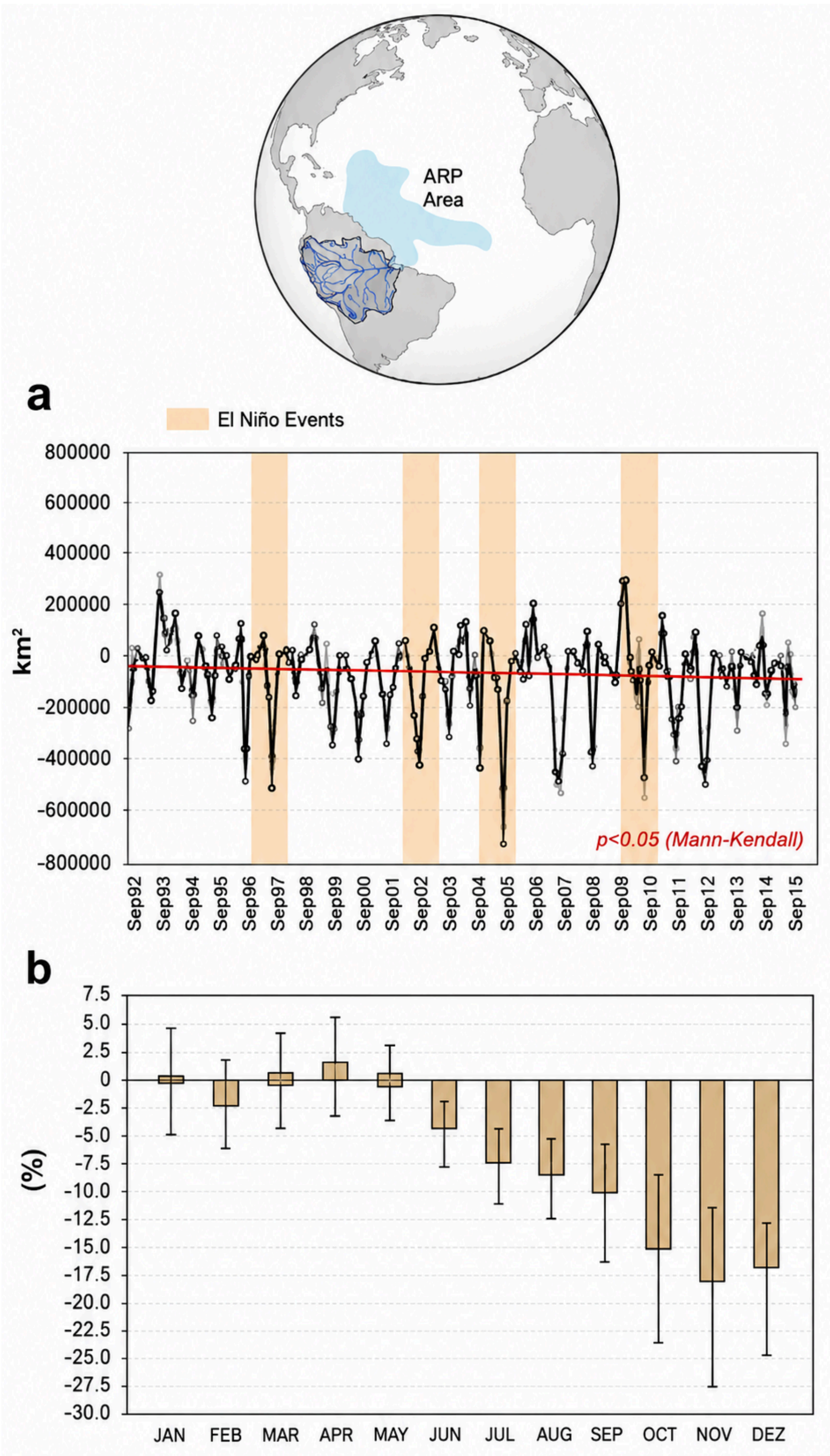

Figure 7

Assessment of changes in the Amazon River plume area

Changes in the Amazon river plume (ARP): (a) difference in total area (km2) between deforestation and control scenarios and annual trend (Mann-Kendall test in red); and (b) monthly percent variation in ARP area between the deforestation and control scenarios. Note that in (a), the El Niño 3.4 years are shaded out.

Supplementary Files

This is a list of supplementary files associated with this preprint. Click to download.

- SupplementaryinformationGouveiaetal2026.docx